Fluid-structure interaction of a 7-rods bundle

Benchmarking numerical simulations with experimental data

Bertocchi, F.; Rohde, M.; De Santis, D.; Shams, A.; Dolfen, H.; Degroote, J.; Vierendeels, J.

DOI
10.1016/j.nucengdes.2019.110394

Publication date
2020

Document Version
Final published version

Published in
Nuclear Engineering and Design

Nuclear Engineering and Design 356 (2020) 110394

Contents lists available at ScienceDirect

Nuclear Engineering and Design

journal homepage: www.elsevier.com/locate/nucengdes

Fluid-structure interaction of a 7-rods bundle: Benchmarking numerical simulations with experimental data

F. Bertocchi[a,*], M. Rohde[a], D. De Santis[b], A. Shams[b], H. Dolfen[c], J. Degroote[c,d], J. Vierendeels[c]

[a] Faculty of Applied Sciences, Department of Radiation Science and Technology, Delft University of Technology, Mekelweg 15, 2629 JB Delft, The Netherlands
[b] Nuclear Research and Consultancy Group (NRG), Westerduinweg 3, 1755 LE Petten, The Netherlands
[c] Department of Flow, Heat and Combustion Mechanics, Ghent University, Sint-Pieternieuwstraat 41, B-9000 Ghent, Belgium
[d] Flanders Make, Belgium

A B S T R A C T

Fluid flows through rod bundles are observed in many nuclear applications, such as in the core of Gen IV liquid metal fast breeder nuclear reactors (LMFBR). One of the main features of this configuration is the appearance of flow fluctuations in the rod gaps due to the velocity difference in the sub-channels between the rods. On one side, these pulsations are beneficial as they enhance the heat exchange between the rods and the fluid. On the other side, the fluid pulsations might induce vibrations of the flexible fuel rods, a mechanism generally referred to as Flow Induced Vibrations (FIV). Over time, this might result in mechanical fatigue of the rods and rod fretting, which eventually can compromise their structural integrity. Within the SESAME framework, a joint work between Delft University of Technology (TU Delft), Ghent University (UGent), and NRG has been carried out with the aim of performing experimental measurements of FIV in a 7-rods bundle and validate numerical simulations against the obtained experimental data. The experiments performed by TU Delft consisted of a gravity-driven flow through a 7-rods, hexagonal bundle with a pitch-to-diameter ratio P/D = 1.11. A section of 200 mm of the central rod was made out of silicone, of which 100 mm were flexible. Flow measurements have been carried out with Laser Doppler Anemometry (LDA) whereas a high-speed camera has measured the vibrations induced on the silicone rod. The numerical simulations made use of the Unsteady Reynolds-averaged Navier-Stokes equations (URANS) approach for the turbulence modelling, and of strongly coupled algorithms for the solution of the fluid-structure interaction (FSI) problems. The measured frequency of the flow pulsations, as well as the mean rod displacement and vibration frequency, have been used to carry out the benchmark.

1. Introduction

In nuclear applications, rod bundle geometries are very common configurations which can be found in heat exchangers, in the core of Liquid Metal Fast Breeder Reactors (LMFBR), Pressurized Water Reactors (PWR), Boiling Water Reactors (BWR) or Canadian Deuterium reactors (CANDU). When a fluid flows in the space between the rods, a velocity difference between the low-speed region in the rod gap and the bulk occurs. The shear between these two regions can trigger streaks of large coherent structures carried by the flow (Lexmond et al., 2005; Mahmood, 2011), also known as gap vortex streets. The mechanism responsible for their formation is not yet fully understood, and different theories have been proposed. If the velocity profile across the gap has an inflection point, a linear instability mechanism may be triggered, as discussed in Tavoularis (2011), Guellouz and Tavoularis (2000), Moradi and Tavoularis (2019) and Merzari and Ninokata (2011), which leads to the formation of the gap vortex streets. The inflection point in the velocity profile is regarded as a necessary (although not sufficient) condition for these periodical vortices to form, as predicted by the Rayleigh's criterion (Rayleigh, 1879). Many experiments on gap vortex streets in rod bundle flows have been done in the past (Rowe et al., 1974; Rehme, 1987; Möller, 1991) and recently (Choueiri and Tavoularis, 2014; Choueiri and Tavoularis, 2015; Piot and Tavoularis, 2011). An extensive review on the subject was provided by Meyer (2010). Because of the increase in computer power, Computational Fluid Dynamics (CFD) studies have also been performed to study these phenomena. For example, some of the first Unsteady Reynolds-averaged Navier–Stokes equations (URANS) simulations were performed by Chang and Tavoularis (2005) and Chang and Tavoularis (2007) and Large Eddy Simulations (LES) were performed by Merzari and Ninokata (2009) and Merzari and Ninokata (2011). The gap vortex streets can be beneficial due to the enhanced heat exchange between fuel rods and nuclear coolant, which prevents hot spots on the outer cladding of the fuel elements.

However, the vortex streets can be responsible for flow-induced vibration (FIV) which can cause wear, rod failure and fuel leakage. In the past few decades, the study of FIV of slender bodies in axial flow has relied on simplified analytical models; a review of such models was provided by Paıdoussis (2014) and Paıdoussis (2016). From the experimental point of view, measuring the small rod vibrations in

* Corresponding author.
E-mail address: F.Bertocchi@tudelft.nl (F. Bertocchi).

https://doi.org/10.1016/j.nucengdes.2019.110394
Received 9 May 2019; Received in revised form 18 September 2019; Accepted 21 October 2019
Available online 31 October 2019

Nomenclature

Latin symbol	Description(Dimension)
D	rod diameter (m)
E_{sil}	silicone Young modulus (Pa)
f_{str}	flow pulsation frequency (Hz)
f_{wall}	vibration frequency (Hz)
L_{dev}	development length (m)
L_{sil}	silicone rod length (m)
P/D	pitch-to-rod diameter ratio
W/D	nearest wall distance-to-rod diameter ratio
Q	flow rate ($m^3 s^{-1}$)
t_{FEP}	FEP wall thickness (m)
t_{PMMA}	Pespex wall thickness (m)
t_{sil}	silicone wall thickness (m)
y_w^+	non dimensional height of the mesh 1st cell
α	flow distributor's divergent angle (°)
Δt	time step (s)
Δz^+	mean stream-wise mesh resolution
$\bar{\varepsilon}$, ε	mean and instantaneous vibration displacement (m)
λ	flow pulsation wavelength (m)
μ	water dynamic viscosity (Pa s)
ν	silicone Poisson ratio
ρ	water density (kg m^{-3})
ρ_{sil}	silicone density (kg m^{-3})

Non dimensional number	Description
Re	Reynolds
CFL	Courant-Friedrichs-Lewy
ALE	Arbitrary Eulerian–Lagrangian
BWR	Boiling Water Reactor
CANDU	Canada Deuterium Uranium
CFD	Computational Fluid Dynamics
CMOS	Complementary Metal-Oxide Semiconductor
CSM	Computational Structural Mechanics
FEP	Fluorinated Ethylene Propylene
FIV	Flow-Induced Vibration
FFT	Fast Fourier Transform
FSI	Fluid–Structure Interaction
DFT	Dicrete Fourier Transform
LDA	Laser Doppler Anemometry
LES	Large Eddy Simulation
LMFBR	Liquid Metal Fast Breeder Reactor
PMMA	Polymethyl Methacrylate
PWR	Pressurized Water Reactor
RANS	Reynolds-Averaged Navier–Stokes
SEEDS − 1	SEven rods bundle Experiment in Delft for Sesame
URANS	Unsteady Reynolds-Averaged Navier–Stokes

complex fuel assemblies can be extremely challenging. Furthermore, the results can be affected by uncertainties on experimental parameters, such as rod constraints and operational conditions. Numerical Fluid-Structure Interaction (FSI) simulations based on the use of CFD and Computational Structural Mechanics (CSM) represents an alternative to the classical theoretical models and can complement the experimental measurements. For example, in De Ridder et al. (2013) and De Ridder et al. (2015) the work focused on slender solitary rod, and the structural part of the FIV problem was modelled with three-dimensional solid elements; a URANS approach was used for modelling the turbulent flow. In De Santis and Shams (2017), URANS simulations were carried out on single rods and rod bundles, extracting the natural frequency and the damping ratio of the system. FSI simulations of a large fuel assembly remain very challenging and computationally expensive. Nevertheless, they could be extremely helpful to shed light on the mechanisms responsible for the flow-induced vibration and fluid-dynamic instabilities in fuel assemblies. Therefore, it is important to validate the numerical tools against experimental data.

This work aimed at benchmarking the tools and models developed by Ghent University and NRG with experimental data generated at Delft University of Technology.

The experimental facility consisted of a gravity-driven water loop with a 7-rods hexagonal bundle whose pitch-to-diameter ratio (P/D) was 1.11. Only a section of 100 mm of the central rod, made out of silicone, was flexible. Flow measurements were carried out with Laser Doppler Anemometry (LDA) whereas a high-speed camera measured the vibrations induced on the silicone rod to extract displacement frequency and amplitude. The optical access to the central rod of the bundle was ensured by using Fluorinated Ethylene Propylene (FEP) to match the water's refractive index. As for the numerical part, the flow equations were solved with a finite volume method on deforming grids by means of the Arbitrary Eulerian-Lagrangian approach (ALE). Ghent University adopted Ansys Fluent (v 17.0) for the flow calculations, where unsteady Reynolds-averaged Navier-Stokes (URANS) equations with a $k-\omega$ SST model were solved. A finite element method implemented in Abaqus (v 6.14) was used for the structure. The coupling between the flow simulation and the structural deformation was done with an in–house code, applying a quasi-Newton algorithm. NRG performed numerical simulations using the Star CCM + (v 11.06) code with the URANS approach, and the $k-\omega$ SST turbulence model. The finite element method was used to solve the linear elastic problem for the structure. The two solvers were tightly coupled with the Gauss-Seidel method. The configuration corresponding to a Reynolds number of 10100 (based on the bundle hydraulic diameter) and mass flow rate of 2.14 kg s^{-1} was chosen as a test case for the validation. The measured frequency of the coherent structures in the flow, as well as the mean rod displacement and vibration frequency, were used to carry out the benchmark study.

2. Experimental setup

2.1. Test loop

The SEEDS − 1 (SEven rods bundle Experiment in Delft for Sesame) experimental loop consisted of a water loop with a 7-rods hexagonal bundle, where the central rod had a section made of flexible silicone rubber. The bundle was enclosed inside an outer casing of transparent polymethyl methacrylate (PMMA). The water flowed by gravity from an upper vessel through the bundle and was collected in a lower tank, where it was recirculated by a centrifugal pump. A valve with a linear response adjusted the flow rate, which was monitored by a magnetic flow meter (ABB - type HA3) and by an ultrasonic flow meter (model TTFM100-B-HH-NG, B. M. Tecn. Industriali) independently.

2.2. Hexagonal rod bundle

In order to expect vibrations induced by periodical flow pulsations, the length of the flexible silicone must be comparable with the wavelength of the expected flow oscillations. If the rod is too long compared to the size of the pulsations, their effects would cancel out and no flow-induced oscillation would be measurable. A work from Gent University (De Ridder et al., 2016), with a P/D ratio of 1.11, had showed that these flow pulsations were expected to have a length of 70 mm. The total length of the silicone rod was 200 mm, of which 100 mm has to be considered the flexible section because the two end of the silicone tube were slid over the stainless steel rod for a length of 50 mm each. The main parameters of the hexagonal lattice and of the test section are listed in Table 1. The sketch of the hexagonal test section casing and of

Table 1
Bundle's main dimensions, including the available dimensional tolerances. D: outer rod diameter, P/D: pitch-to-diameter ratio, W/D: nearest wall distance -to-rod diameter ratio, α: half-aperture angle of the flow distributor, t_{PMMA}: Perspex wall thickness; L_{dev}: development length upstream of the optical window, t_{FEP}: FEP wall thickness.

Hexagonal lattice	Design parameters
$D = (30 \pm 0.1)$ mm	$\alpha = 4°$
$P/D = 1.11$	$t_{PMMA} = (6 \pm 0.4)$ mm
$W/D = 1.11$	$L_{dev} = 1.5$ m
	$t_{FEP} = 0.25$ mm

the inlet distributor flange are shown in Fig. 1. The flow entered the hexagonal bundle via a flow conveyer that distributed the water over the subchannels (Fig. 1(b)). Downstream the flow conveyer, a development length L_{dev} of 1.5 m) was added before reaching the measurement section. The internal structure of the flow distributor had a two-fold function. It broke the large vortices that might form in the stream, thus mixing the flow, and it redistributed the fluid uniformly among the subchannels. Flow detachment from the wall of the distributor was avoided with a divergent angle of 4° (Idel'chik, 1966).

The optical access near the central rod was achieved by partially replacing the stainless steel with FEP around the front rods, as shown in Fig. 2. FEP was already employed in Dominguez-Ontiveros and Hassan (2009), Mahmood (2011), Bertocchi et al. (2018). All the rods were filled with water to prevent the FEP (in the surrounding rods) and the silicone (in the central one) from collapsing under the fluid's pressure, and to minimise light refraction during the measurements.

3. Measurement system

This section describes the measurement systems used in the experiments, consisting of the LDA system and the high-speed camera.

3.1. Laser doppler anemometry

A 2-component LDA system (DANTEC, Denmark) with a maximum power of 300 mW was used for measuring the flow. The water was seeded with particles to scatter the light once they travelled through the sensitive region of the laser beam pair, which was an ellipsoidal probe of 0.02 mm^3. Borosilicate glass hollow spheres (LaVision, Germany) with an average density of 1.1 gm^{-3} and a diameter of 9–13 µm were used. The LDA system was moved in position with a traverse system. LDA measurements were conducted in the middle of the hexagonal transparent section, moving the laser probe from a position close to the outer wall towards the central rod, as shown by the dashed line in Fig. 2b. The 95% confidence level was evaluated for the mean stream-wise velocity: its width was as low as 0.5% for all the measurement cases.

The flow rate was adjusted within the range 1.05–4.8 kg s^{-1}. The frequency spectra were evaluated by means of the slotting technique (Mayo, 1974; Tummers and Passchier, 2001; Tummers and Passchier, 1996), where sample pairs detected within a certain time interval (lag time) were allocated into the same slot. The product of the velocities of each sample pair (cross-product) was calculated and the average value of the correlation was taken within each slot. The slotting technique omitted the cross-products with zero lag time (self-products), reducing the uncorrelated noise. The amount of particles going through the probe volume is higher for faster particles, biasing the spectrum (Adrian and Yao, 1986). Hence, their contribution to the spectrum would be higher than the real one. Therefore, the transit time weighting algorithm was implemented to reduce this effect (Nobach, 2002). An example of the frequency spectrum of the stream-wise velocity component of the flow is shown in Fig. 3a.

3.2. High speed camera

A Complementary Metal-Oxide Semiconductor (CMOS) camera Imager MX 4M (LaVision, Germany) was used to record flow-induced vibrations of the rod. The FIV tracking system could not have both edges of the rod in focus with sufficient resolution because the camera should have been moved too far from the target. The camera was, thus, focused on one edge and recorded 15000 images at 300 frames per second in each measurement. The contrast between the white silicone and the dark background was enhanced with a flash light, and by keeping the setup in the dark. A binary filter converted the intensity values of the light in the frames into ones or zeros, based on the Otsu algorithm (Otsu, 1979). The white silicone was a region of "ones", while the background corresponded to "zeros". The location of the vertical border between the two regions of the filter represented the edge of the rod. A sample of a raw image and of the corresponding intensity map is shown in Fig. 4. Each pair of consecutive edge positions was used to obtain the instantaneous displacement of the rod edge on the plane orthogonal to the line of sight of the camera, sketched in Fig. 4b. The series of instantaneous displacements gave the average displacement $\bar{\varepsilon}$, which was calculated as

$$\bar{\varepsilon} = \frac{1}{N-1} \sum_{i=1}^{N-1} \varepsilon_i, \tag{1}$$

where N is the number of recorded images and ε_i is the i-th displacement value. The frequency spectrum of the displacement of the silicone rod was estimated in two ways: by means of the Fast Fourier Transform (FFT), and by evaluating the autocorrelation function of $\varepsilon(t)$. The frequency at which periodical oscillation of the rod occurred was revealed in the frequency spectrum by a peak. The Bartlett's method was applied to reduce the noise in the spectra (Monson, 1996). An example of frequency spectrum of the vibrations measured on the silicone rod is

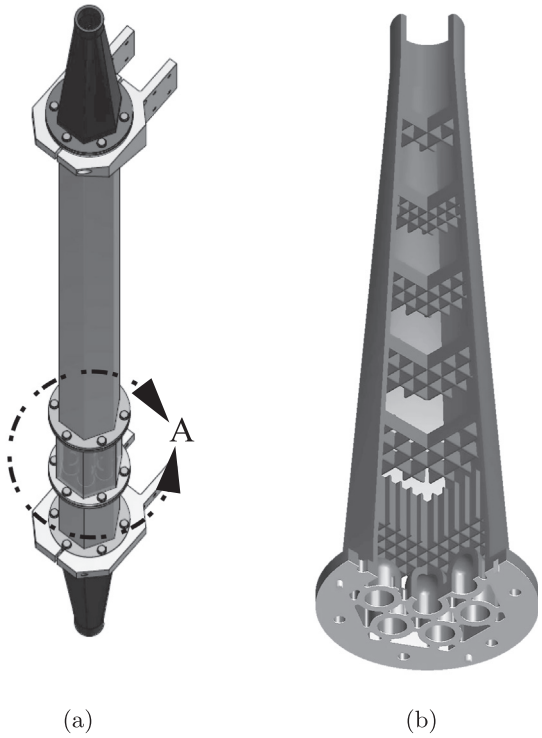

Fig. 1. a) An outer hexagonal casing, containing the rod bundle, is clamped to the supports. The LDA measurements are performed at the location of the transparent Perspex casing (detail A). b) The inlet flow distributor conveys the fluid in the subchannels of the bundle; its internal structure breaks large vortices developed in the fluid falling from the top vessel.

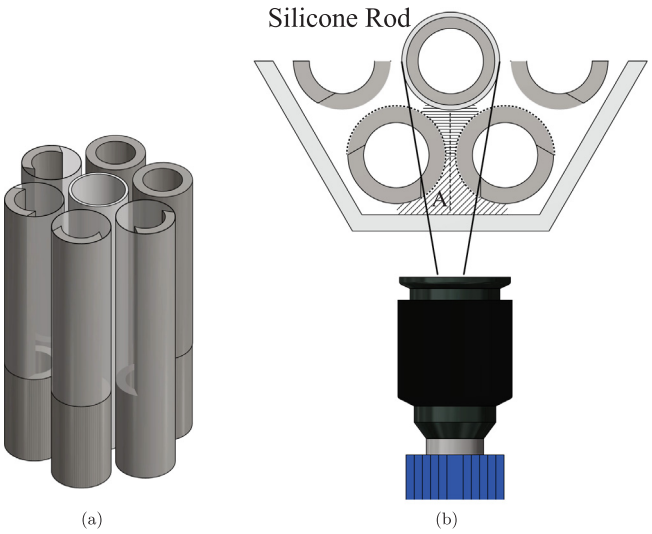

Fig. 2. a) View of the optical window where the FEP rods are visible. b) Top view of half of the hexagonal bundle geometry. The dashed profile on the rods represents the FEP used to match the refractive index of water; the straight hatched line represents the LDA measurement positions. Horizontal hatching: central subchannel. Diagonal hatching: edge subchannel. The rods are filled with water to avoid image distortion through FEP.

shown in Fig. 3(b). The peak in the spectrum based on the auto-correlation function was fitted with a Gaussian bell to obtain a mean value of the frequency.

4. Case study

This section presents an overview of the experimental results, from which the case study for the benchmark was chosen. The experimental results are reported against the bundle Reynolds number, which was based on the total bundle flow area. Fig. 5(a) reports the stream-wise rate of passage of the coherent structures f_{str}. This was estimated from the spectral analysis of the LDA measurements. Fig. 5(a) shows that the frequency of flow pulsations in the stream-wise direction increases almost linearly with the Reynolds number, as observed also in Bertocchi et al. (2019). This is because the flow pulsations move faster axially through the measurement laser probe as the flow rate increases.

The wavelength of the flow pulsations was estimated based on Taylor's hypothesis: the flow oscillations were considered as steady and "frozen" entities carried by the main flow (Nieuwstadt et al., 2015). Fig. 5(b) shows the stream-wise wavelength of the structures λ, which appears to be independent of the Reynolds number, consistently with the findings of Meyer and Rehme (1995), Mahmood (2011) and Bertocchi et al. (2018).

The frequency of oscillation of the rod f_{wall}, measured with the high-speed camera, is shown in Fig. 6(a). The frequency reached a maximum of 4.14 Hz and it decreased at higher flow rates. An increased magnitude of the oscillations, shown in Fig. 6(b), was found in the same Reynolds number range, which could be due to the fluctuating pressure field caused by the flow pulsations that synchronizes with the rod motion. If the Reynolds number is increased beyond this range, the magnitude of the displacements decreases by a factor two as the synchronization condition may have died out. The distribution of experimental points reported in Fig. 6(b) shows some degree of scattering for Re>15000. This is because the magnitude of the displacements is below the pixel accuracy of the camera (≈ 9 μm).

A mass flow rate of 2.14 kg s^{-1} was chosen as the case study, where a rod mean displacement of 14μm was measured. The experimental conditions are listed in Table 2.

5. NRG's numerical approach

5.1. Numerical validation of the fluid domain

Numerical simulations of the SEEDS − 1 test section were performed with the commercial code STAR-CCM + (STAR CCM + v, 2016). In the experimental setup, water flowed from the top to the bottom of the test section due to gravity and it entered the test section via a mixing flow distributor previously shown in Fig. 1(b). The flow distributor was used as mixing device, therefore the inflow boundary conditions were not well known at the inlet. Hence, an upstream domain with inflow-outflow periodic boundary was chosen to generate more realistic inflow conditions for the FSI problem. This solution provided a well-defined inlet velocity profile at the inflow section, in correspondence of the flexible rod. Furthermore, the periodic boundary conditions allowed for a shorter upstream domain than that of the experimental setup, reducing, thus, the computational effort.

A shorter domain, however, could affect the flow field, so different domain lengths were tested, namely L = 600 mm, 1000 mm, and 1500 mm. The frequencies of the flow pulsations and the experimental values were compared in order to identify the shortest domain for

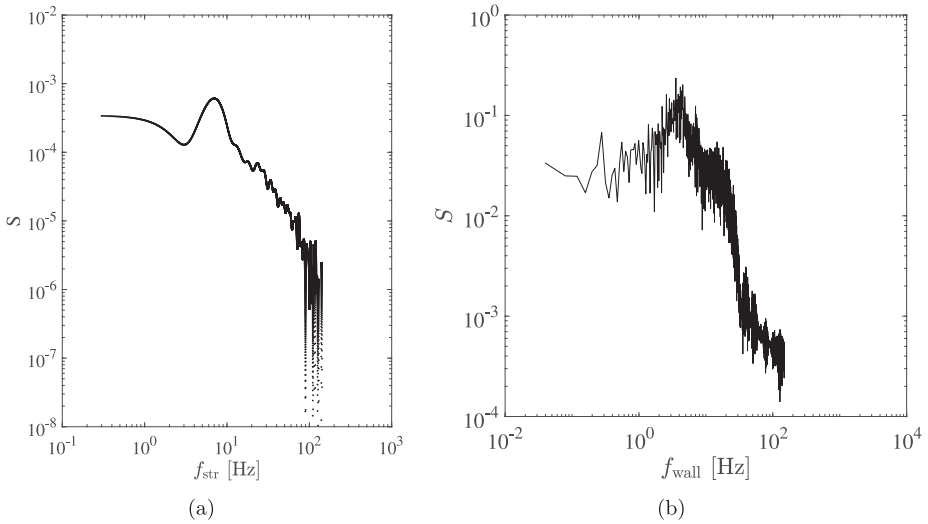

Fig. 3. a) Frequency spectrum computed from the LDA measurements for a flow rate of 2.14 kg s^{-1}: a peak is visible at 6.9 Hz. b) FFT of the vibration amplitude of the silicone rod wall.

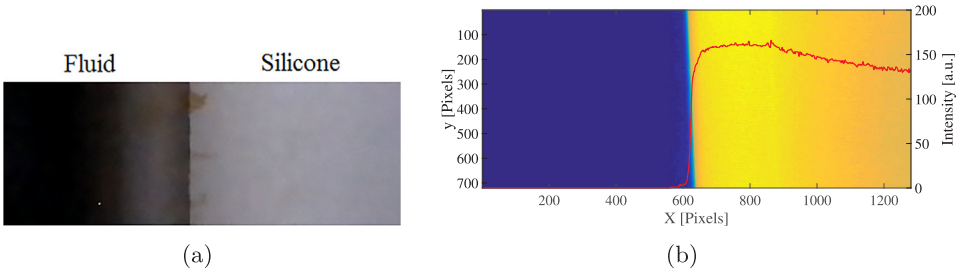

Fig. 4. a) Sample image of the edge of the silicone rod with dark background. b) Light intensity map with plot of the numeric values along the horizontal line $y = 400$.

which the effects of the domain length were negligible. Only the fluid domain was considered in the simulations to study the characteristic of the flow pulsations, i.e., the rods were assumed rigid. The cross-section of the computational domain is reported in Fig. 7. Periodic boundary conditions were applied at the inflow/outflow sections of the domain and no-slip wall boundary conditions were imposed on the remaining surfaces of the computational domain.

Water at 25 °C was used as working fluid, whose density and viscosity were $\rho = 997\,\mathrm{kg\,m^{-3}}$ and $\mu = 8.94 \times 10^{-4}\,\mathrm{Pa\,s}$, respectively. A constant mass flow rate of $2.14\,\mathrm{kg\,s^{-1}}$ was applied, which resulted in a Reynolds number $\mathrm{Re} = 9700$ based on the bulk velocity and the hydraulic diameter. All the simulations were performed using the URANS approach with the $k - \omega$ SST turbulence model and a constant time step $\Delta t = 1\,\mathrm{ms}$, which corresponded to a maximum Courant-Friedrichs-Lewy (CFL) number of ≈ 0.5. A wall-resolved computational grid was generated for the problem. The grid consisted of hybrid polyhedra-prism layers on the cross-section extruded in the stream-wise direction to generate the 3D mesh. A cross-sectional mesh of 25600 elements with a mean wall-normal height of the first cell $y_w^+ \approx 0.6$ was selected after a preliminary mesh sensitivity study. The 2D cross-sectional mesh was extruded in the stream-wise direction using a constant spacing of the elements, which corresponded to a mean stream-wise grid resolution of $\Delta z^+ \approx 100$. 151, 251 and 377 stream-wise divisions were used for the cases with L = 600 mm, 1000 mm and 1500 mm, respectively.

Due to the small P/D of the configuration, strong velocity pulsations with a characteristic frequency appeared in the rod gaps. These velocity pulsations are clearly visible in Fig. 8, where the instantaneous contours of the velocity magnitude are reported for the three domain lengths on the horizontal section (Section H in Fig. 7). Although all the domains resulted in a well-developed fluid flow, a more quantitative analysis to select the proper length of the computational domain was required. A similar numerical study on the domain length is described in Merzari et al. (2008). For this reason, the frequency of the velocity signal was analysed at three different locations shown in Fig. 9(a) on the cross-sectional plane. The frequency was computed with the FFT algorithm of the temporal velocity signal. Furthermore, for each location, the velocity was monitored at three positions along the stream-wise direction, namely near the inflow section, near the outflow section and at the middle of the domain. For all the simulations, it was observed that the computed frequencies were the same at all the locations throughout the domain, meaning that the flow pulsations in the fluid domain were well developed. The computed frequencies are reported in Table 3 together with the average experimental value (SESAME, 2017).

The shortest domain (L = 600 mm) over-predicted the frequency of the velocity fluctuations, suggesting that a length of 600 mm affected the velocity pulsations. On the other hand, the frequencies computed in the longer domains agreed very well with each other and were also close to the experiments. Therefore, the numerical model could correctly reproduce the physics of the problem for these two cases. Since L = 1000 mm and L = 1500 mm gave a similar frequency, L = 1000 mm was considered sufficient to minimize the numerical effects, so it was used to generate proper inflow boundary conditions for the FSI problem.

5.2. FSI analysis

In this section, the FSI analysis of the SEEDS − 1 experiment is discussed. Only the silicone rod was flexible, while the stainless steel rods could be practically assumed as rigid bodies. Therefore, from the modelling point of view, the structural domain took into account only the silicone rubber rod. The length of the silicone rod used in the experiments was 200 mm, of which only 100 mm was flexible (see Table 2). In the numerical model, the two extremities of the 100 mm long silicone tube were perfectly clamped, hence no displacement of these surfaces was allowed.

Since the flexible rod experienced very small displacements (of the order of micrometers), the structure could be modelled as an elastic solid whose material properties are listed in Table 2. The flexible part of the rod was modelled in STAR-CCM + using a linear finite element method and an implicit Newmark's time integration scheme. Moreover, linear deformations and linear elastic material properties are used. The computational mesh used for the rod is shown in Fig. 9b; it contained hexahedral elements with 5, 80, and 150 divisions along the radial, circumferential and stream-wise directions, respectively. A co-simulation was used to generate well-developed inflow fluid boundary conditions for the FSI simulation.

The computational domain can be divided into three main regions:

- **Upstream sub-domain** Previously derived from the study on flow pulsations (Fig. 8, L = 1000 mm); recirculation boundary conditions

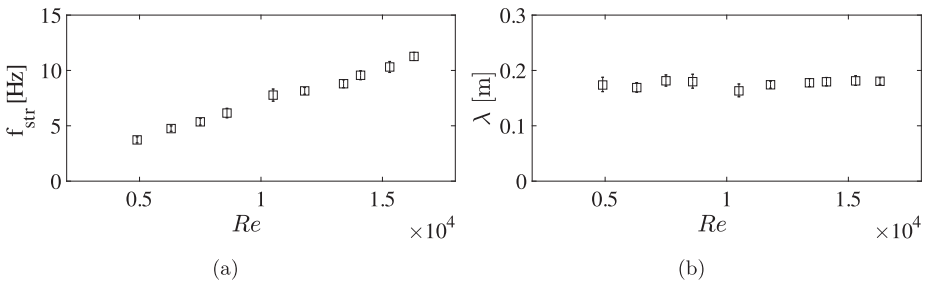

Fig. 5. a) Average rate of passage of coherent structures along the stream-wise direction for the central subchannel. b) Average wavelength of the structures along the stream-wise direction for the central subchannel based on Taylor's hypothesis.

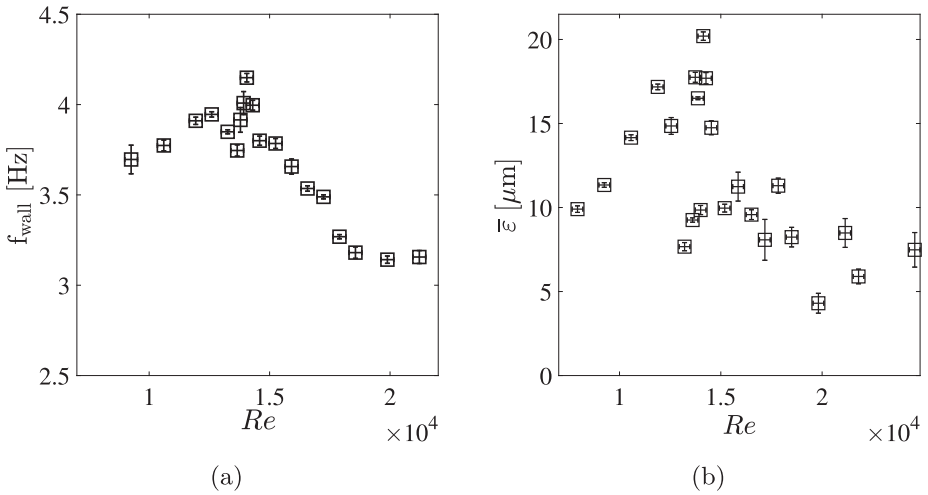

Fig. 6. a) Response frequency and b) mean displacement of the rod against the Reynolds number based on the near-wall subchannel flow area (edge subchannel).

Table 2
Material properties of the silicone rod with dimensional tolerances, where available: ρ_{sil} silicone density, ν Poisson's ratio, E_{sil} Young's modulus, L_{sil} flexible length of silicone, t_{sil} silicone rod wall thickness. Experimental conditions adopted as reference case: Q volumetric flow rate, Re Reynolds number, $\bar{\epsilon}$ mean displacement, f_{wall} frequency of oscillation of the rod, f_{str} frequency of coherent structures in the axial direction.

Silicone properties		Experimental conditions	
ρ_{sil}	1180 kg m^{-3}	Q	2.14 × 10^{-3} m^3 s^{-1}
ν	0.48	Re	10100
E_{sil}	1 MPa	$\bar{\epsilon}$	14 µm
L_{sil}	(100 ± 5) mm	f_{wall}	3.8 Hz
t_{sil}	(1.5 ± 1) mm	f_{str}	7.8 Hz

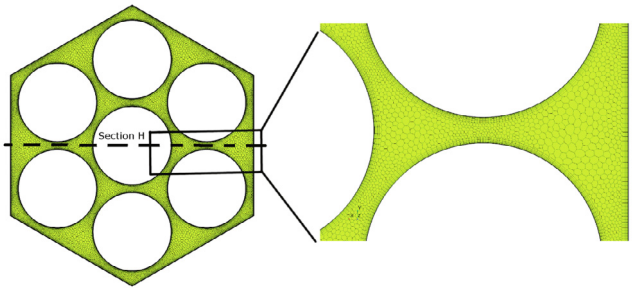

(a)

Fig. 7. Cross-sectional view of computational grid together with close up view around the rod gap.

were applied, and only a fluid problem was solved.

- **FSI sub-domain** It included the flexible rod, shown in more detail in Fig. 11. This sub-domain was 100 mm long and consisted of six rigid rods surrounding a flexible one in the centre. The velocity profile at the inlet section of the sub-domain was mapped from the outlet of the upstream sub-domain. No boundary condition was applied at the interface between the upstream and the FSI sub-domain. All the internal surfaces of the FSI section were treated as no-slip walls. Furthermore, the surface of the middle rod was treated as a flexible wall and FSI compatibility conditions were applied, while the remaining walls were considered rigid. The cross-sectional fluid mesh was the same used in the upstream recirculation sub-domain, while 87 subdivisions were used in the stream-wise direction, with a resulting stream-wise mesh resolution of $\Delta z^+ \approx 30$.
- **Outflow sub-domain** It was 100 mm long and it reduced the effects of the outlet boundary conditions on the solution of the FSI sub-domain. It contained only rigid rods, hence only a fluid problem was solved. The inlet section was an internal interface, hence no boundary condition was imposed. On the other hand, a pressure outlet boundary condition was imposed at the outflow section. The remaining surfaces of the sub-domain were treated as rigid walls. The cross-sectional fluid mesh was the same used in the upstream sub-domain, while in the stream-wise direction 20 subdivisions were used.

In the experimental setup, the rods were filled with stagnant water to prevent the silicone rod from collapsing under the effect of the fluid's external pressure. The numerical simulations initially considered the filling material of the central rod as a solid with properties similar to the water, and with the length of the flexible portion of the silicone rod, whose scheme is shown in Fig. 11a. However, this approach was abandoned since it introduced too many uncertainties on the values of the material properties. Moreover, from preliminary FSI simulations, it was observed that it would considerably over-estimate the rigidity of the rod. An alternative way of modelling the internal fluid was then pursued.

5.2.1. Additional modelling of the filling

A more realistic modelling of the filling would take into account the actual fluid within the rod. For this reason, the computational domain was modified as in Fig. 10b. This model and the one previously shown in Fig. 10a were similar except for the additional fluid domain added to account for the water filling the central rod. This additional domain consisted of a cylinder of stagnant water at atmospheric pressure with a diameter of 27 mm (i.e. the inner diameter of the silicone rod) and length of 1980 mm (i.e. the length of the water column in the experiments, including the downstream length). This choice was made in order to keep the configuration as close as possible to the experiments and to avoid spurious pressure fluctuations between the two extremities in the case of a short domain.

The portion in contact with the inner wall of the flexible rod was assumed to be a deforming no-slip wall. The remaining surfaces were considered as fixed no-slip walls. Due to the fact that the filling fluid was displaced only by the small oscillations of the silicone rubber rod, the magnitude of the velocities expected within this domain was small. Therefore, a coarse mesh for the filling was used to reduce the computational cost. The adopted cross-sectional mesh consisted of approximately 500 polyhedrons with a prism layer near the wall; this mesh was then extruded in the stream-wise direction using 500 divisions. The material properties of the filling were the same of water in

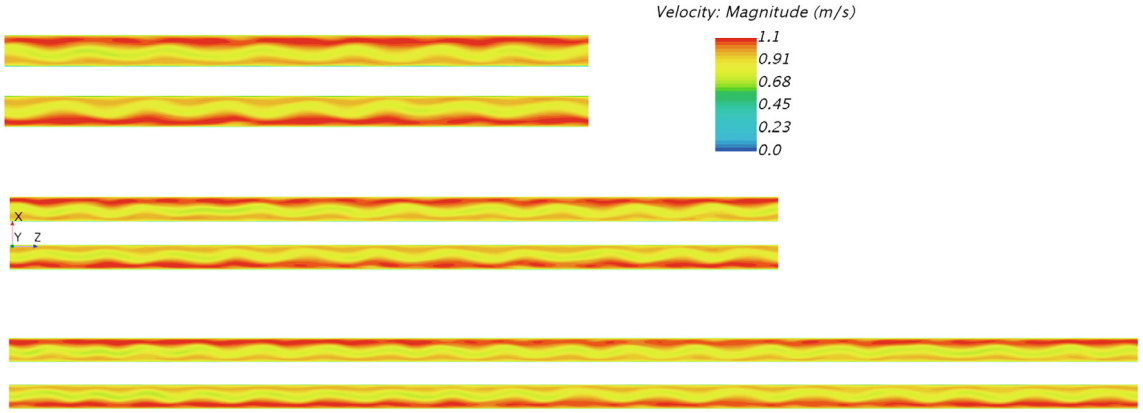

Fig. 8. Instantaneous velocity contours on the middle section (H) for different lengths of the domain. From top to bottom: L = 600 mm, 1000 mm and 1500 mm.

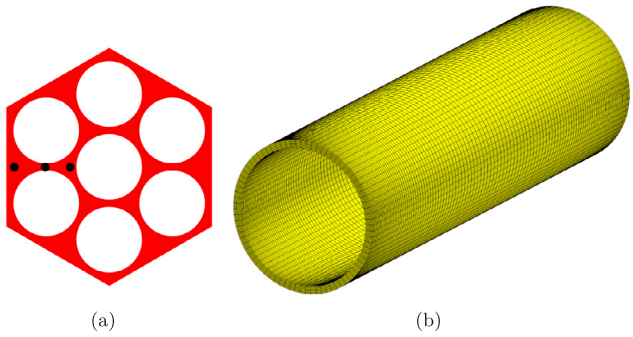

Fig. 9. a) Locations used to measure the frequency of the velocity pulsations. b) Structural mesh for the flexible silicone rubber rod.

Table 3
Frequencies of the velocity pulsations computed with different lengths of the domain and average frequency measured in the experiment.

L = 600 mm	L = 1000 mm	L = 1500 mm	Experimental
9.4 Hz	8.6 Hz	8.5 Hz	7.8 Hz

the main fluid domain.

6. Ghent University's numerical approach

The numerical approach consisted of two parts: the first focused on simulating the flow, and the second considered the fluid-structure interaction.

6.1. Flow simulation

The geometry of the experiment was first created in a simplified form for CFD simulations. The Fluent CFD code with the finite volume method was used. The mesh was entirely built with hexahedral cells. Along the circumference of the cylinder, 120 divisions were used, 10 divisions in between two rods and 700 divisions in the axial direction. The inlet and outlet of the domain were connected via periodic boundary conditions. A stream-wise pressure gradient, implemented as a source term in the axial momentum equation, was applied to drive the flow. This ensured a fully developed flow throughout the domain, avoiding a flow development region. The pressure gradient was determined by running several times the same simulation, and repeatedly correcting its value until the mass flow rate was within 1% of the desired value of 2.14 kg s^{-1}. The final value was 935.7 Pa m^{-1}. A length of 100 mm was judged sufficient for this mesh, allowing enough vortex street wavelengths to develop. Since steady Reynolds-averaged Navier-

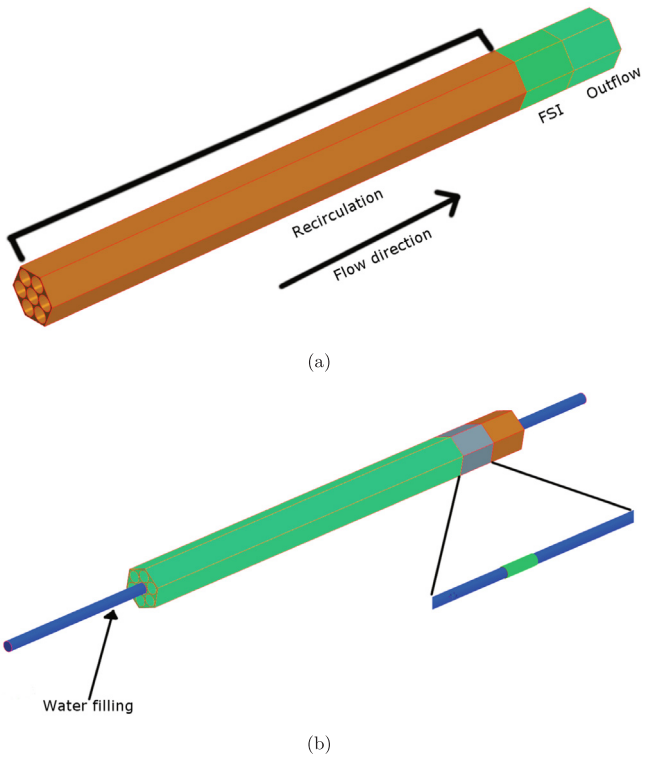

Fig. 10. a) Computational domain used to performed FSI simulations. b) Detail of the FSI sub-domain with the water-filling domain.

Stokes equations (RANS) simulations could not properly predict the fluctuating flow, a URANS approach was followed adopting a $k-\omega$ SST turbulence model, the same approach as chosen by NRG. It has been demonstrated multiple times in the past that URANS is able to capture the gap vortex (De Ridder et al., 2016). A time domain spanning 11 s was discretised into 20000 time steps of 0.55 ms. This corresponded to about 8.5 through-flows of the domain, based on the bulk velocity. The velocity components collected at several points in the domain are stored at every time step. After the simulation, this data were post-processed and the main frequencies were determined.

6.2. FSI analysis

In the second part, a fully coupled FSI simulation was set up. Since the central rod was a hollow tube filled with water, the CFD domain had first to be adapted. Therefore it was closed at the bottom, and connected at the top to the outer domain via a short annular section

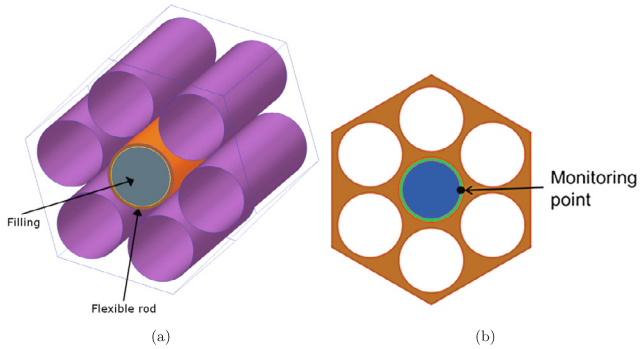

Fig. 11. a) Detail of the FSI sub-domain with a solid filling. b) Monitoring point of the rod displacement.

with a mesh interface. A schematic of the domain is shown in Fig. 12. The silicone tube had an inner diameter of 27 mm, whereas the rest of the domain, corresponding to the steel rod in the experiment, had an inner diameter of 20 mm. The inner domain length of 800 mm was shorter than the real one. Nevertheless it ensured convergence of the coupling iterations. A fairly coarse mesh was used for the inner domain since no major flow phenomena were expected in this region, besides the small axial movement of liquid due to the deformation of the silicone cylinder. As the fluid domain was added afterwards 5000 additional time steps were performed to remove the effect of this change. This stage was used as the initial condition for the FSI calculation. The source term used to drive the flow in the outer domain did not play any role in the inner domain. A length of 1000 mm for the outer CFD domain was considered sufficient to avoid any influence of the deforming silicone part on the upstream flow, due to the re-entering flow perturbations via the periodic boundaries. The silicone rod was considered as the only moving body, which was modelled using a finite element approach with the Abaqus code. The material properties used for the silicone rod are listed in Table 2. 50, 44, and 3 quadratic elements were used for meshing in the axial, circumferential, and radial (wall-normal) directions, respectively. Clamping boundary conditions were applied at both the ends of the silicone rod, which was 100 mm long, corresponding to the actual part of the tube able to deform. The flow and structural solvers were coupled at their mutual interfaces using the IQN-ILS algorithm, which is a quasi-Newton method implemented in the "Tango" in–house code. The time step was increased to 1ms and a total of 1300 FSI time steps were performed. The criterion for convergence relied on the L_2 norm of the vectors of displacements and forces. The difference between the arrays of the current and previous iteration is taken and the L_2 norm of this difference is calculated. The L_2 norm of an array is the square root of the sum of each element squared. When its value drops below a certain threshold (10^{-3} times its value in the first time step), it is considered to be converged.

7. Numerical results

7.1. NRG

Fluid simulations were first performed by considering a rigid structure in order to let the flow field develop. After the flow field was completely developed, the FSI problem was solved with a constant time step $\Delta t = 2.5$ ms. The wall-normal component of the displacement was monitored during the simulation at the point indicated in Fig. 11b, which was at the middle of the flexible rod. The time history of the displacement around the static deformation of the rod is reported in Fig. 13a, and the corresponding estimated frequency of vibration is 6.9 Hz. The main source of excitement of the rod is represented by the velocity pulsations, hence stable and sustained vibrations of the rod are observed, with a frequency close to frequency of the velocity pulsations. However, the vibration frequency is slightly lower due to the added mass contribution of the water filling inside the rod. The frequency spectrum of the oscillating rod is reported in Fig. 13b, where the most energetic peak is at 6.9 Hz. The experimental displacement of the rod is higher than what the simulations predict. In addition, the main frequency of the experimental signal is lower than that observed in the numerical simulations. In particular, the vibration frequency observed in the experiment is 3.8 Hz whereas the frequency observed in the numerical simulations is 6.9 Hz.

7.2. Ghent University

This section analyses the flow velocity obtained from the numerical simulations in order to visualize and to understand the flow instability occurring in the tube bundle. The thick red line in Fig. 14a highlights the plane where a post-processing is done (top view). The instantaneous axial velocity, visualised as contourplot in this plane (Fig. 15), shows that the slow-moving streak of fluid in the gap fluctuates between the outer wall and the central rod. The wavelength of the periodic fluid motion is easily estimated from this figure by counting 12–13 spatial periods within the numerical domain. The corresponding frequency is between 9.3 and 10.1 Hz, based on the convection speed approximated as the bulk velocity of 0.8 m s^{-1}.

The temporal frequency is estimated more precisely via the Discrete Fourier Transform (DFT) of the flow velocity, computed at the black dots shown in Fig. 14a. These points are located at half of the silicone rod and are evenly distributed between the central rod and the outer wall. Fig. 16(a) reports the DFT amplitude of the radial velocity computed at the 5th point from the central rod. This point is located in the middle of the gap between the two peripheral cylinders, where the amplitude of the radial velocity is highest as it does not encounter any obstruction. A peak at 10 Hz confirms the previous estimation, and a second peak occurs roughly at twice the frequency of the first. Higher harmonics in the DFT were also observed by De Ridder et al. (2016). Furthermore, the axial velocity component, which was measured in the experiments, is considered. The clearest axial velocity signals occur

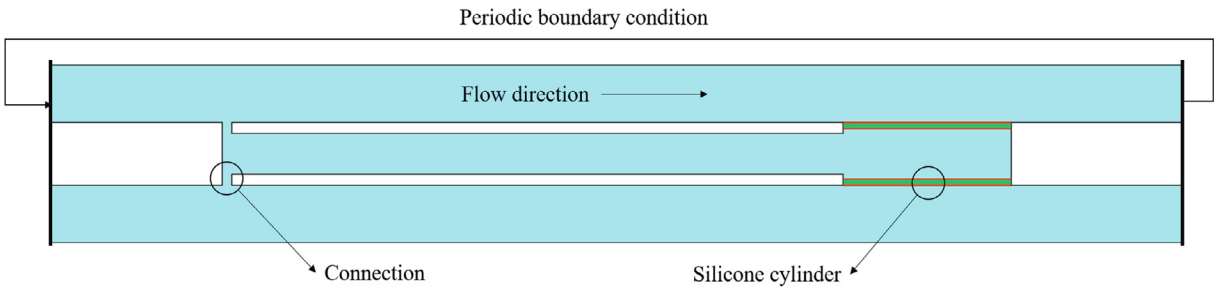

Fig. 12. Schematic of simulation domain (not to scale): cross-section in a plane in between peripheral rods and through the central rod, the fluid domain is indicated in blue, the flexible part of the solid domain in green and the interface in red. Adopted from Dolfen et al. (2019). (For interpretation of the references to colour in this figure legend, the reader is referred to the web version of this article.)

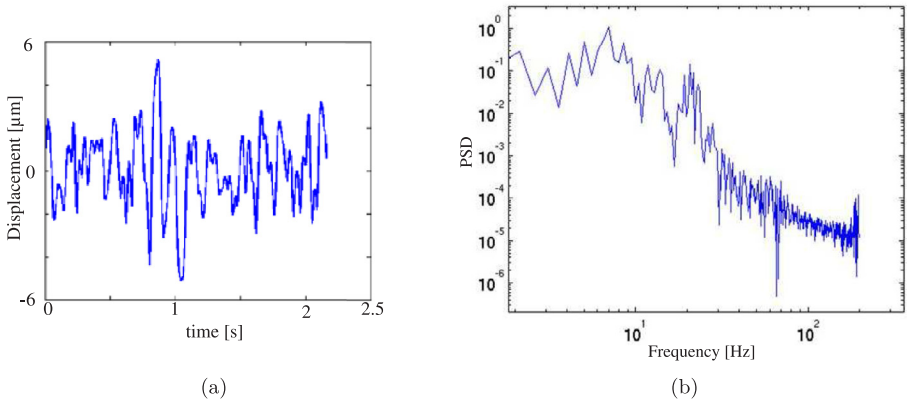

Fig. 13. a) Time displacement history of the monitoring point on the flexible silicone rod. b) Corresponding frequency spectrum.

between the 7th and the 9th position from the central rod, which are located in the bulk of the edge sub-channel, where the mean axial velocity is the highest. Fig. 16(b) shows the DFT computed at the 8th point, which confirms a dominant frequency around 10 Hz. The same value is given by the DFT of the circumferential velocity component (not shown), although quantifying a single dominant frequency is difficult because of the noise embedded in the DFT signal. The dominant frequency computed by this simulation is, thus, around 10 Hz, which is higher than the 7.8 Hz observed in the experiments.

A snapshot of the structural deformation shown in Fig. 14b resembles the lower modes of a vibrating cylindrical shell. The experimental displacement data are retrieved from measurements of a small patch of the silicone rod's surface, facing a rod-to-rod gap. Similarly, the displacement of a single point of the central rod's surface, adjacent to a rod-to-rod gap, is analysed in the numerical simulation. Because of the symmetry in the geometry, six points on the rod's surface are facing a gap, on each side of the hexagon. The radial coordinate of one of these points is plotted as a function of time in Fig. 17(a), where it oscillates around the position at rest (D/2). The DFT of the radial deformation is computed for the six considered points. The first 300 time steps are omitted to avoid any influence from the initialisation. The analysis is limited to 1300 time steps because of computational limitations. This implies that the resolution of the DFT is 1 Hz. The arithmetic average of the six local DFTs is given in Fig. 17(b), where a peak is observed at 10 Hz, the same frequency of the flow pulsation, indicating a forced vibration. However, this does not agree with the experiments, where a vibration frequency of 3.8 Hz was observed. Additionally, the mean amplitude of the displacements is calculated for each of the six points, and then averaged to a single value reported in Table 5. The simulations predict an amplitude that is almost an order of magnitude smaller than the experimental one.

7.2.1. Sensitivity study

This paragraph briefly discusses the sensitivity analysis that was performed as an attempt to explain the mismatch between experiment and simulation. More details on the methodology and results are available in Dolfen et al. (2019).

Firstly, the silicone rod's geometry is investigated. The same simulation performed with a flexible length of 100 mm is repeated for a silicone rod length of 95 mm, obtaining similar DFT amplitude and frequency as the case study. This shows that the tube length has a negligible effect on the deformation. However, a thicker silicone wall (2.5 mm) yields more interesting results in that the vibration amplitude decreases by a factor four. Furthermore, the DFT exhibits multiple dominant frequencies. On top of the peak at 10 Hz, two additional peaks appear at 4 Hz and 17 Hz. It is noteworthy that a frequency of 4 Hz matches the experimental data. The higher frequency of 17 Hz is due to the increased stiffness of the thicker silicone rod.

Given the small bundle's hydraulic diameter (≈ 10 mm), the dimensional tolerances of the components of the test section (rod diameter, Perspex wall thickness) may play a major role. This could lead to an increased bulk velocity up to 18%. Therefore, the influence of the flow rate on the rod's displacement is analysed by performing an additional simulation where the mass flow rate was increased from 2.14 $kg\,s^{-1}$ to 2.53 $kg\,s^{-1}$. As shown in Table 4, the frequency of the vibration increased to 12 Hz, while its amplitude increased to a value of 6.5 μm. This indicates that there is some sensitivity of the vibration to the flow rate. Therefore geometric tolerances could partially explain the observed discrepancy in results.

The following table summarizes the main findings of the benchmark, reporting the experimental results together with the numerical values computed from the simulations performed by NRG and Ghent University.

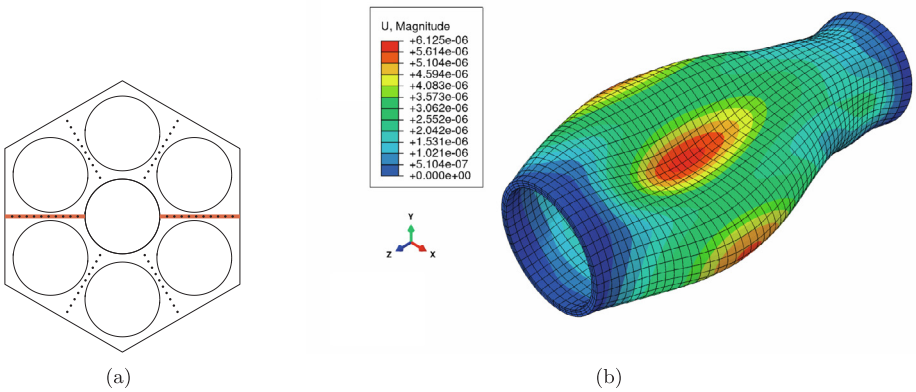

Fig. 14. a) Schematic of the cross-section of the numerical domain; the post-processed points are shown in black and the post-processing plane is indicated in red (as seen from the top). b) Snapshot of the silicone rod deformation; the deformation is scaled by a factor 2000. Adapted from Dolfen et al. (2019). (For interpretation of the references to colour in this figure legend, the reader is referred to the web version of this article.)

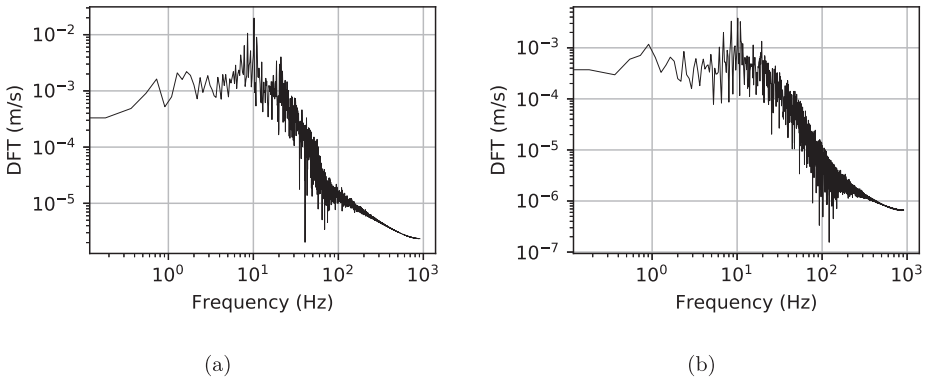

Fig. 15. Contour plot of the axial velocity in the plane indicated by the thick red line in Fig. 14a; the water flows from left to right. Adopted from Dolfen et al. (2019). (For interpretation of the references to colour in this figure legend, the reader is referred to the web version of this article.)

8. Conclusions and recommendations

This work aimed at benchmarking FSI simulations performed by NRG and Ghent University with the experiments carried out at Delft University of Technology. The gravity-driven water flow through a 7-rod hexagonal bundle was measured with LDA to detect the presence of flow pulsations (i.e. coherent structures) in the gap between the rods. A section of the central rod was made of flexible silicone in order to study flow-induced vibrations that were recorded with a high speed camera. The optical access to the surroundings of the central rod was achieved by using FEP, which is a refractive index-matching material, for part of the rods. A reference mass flow rate was selected as the case study for the numerical comparison. The numerical codes used a URANS approach with a $k - \omega$ SST turbulence model for the flow simulations, and strongly coupled algorithms for solving the FSI problem. As for the flow pulsations, both codes agreed reasonably well with the experiments: the computed frequency of the flow pulsations was 8.6 Hz (NRG) and 10 Hz (UGent), compared to the experimental 7.8 Hz. On the other hand, the results of the FSI calculations deviated from the experiments in that they under-predicted the amplitude of the flow-induced vibrations and they over-predicted the respective frequency.

The reason for the mismatch between the numerical and the experimental results is not clear yet. Further investigations are, thus, required. For this reason, the authors would like to put forward the following hypotheses that might lead to an explanation:

- In the numerical simulations, the silicone rubber rod was considered to be perfectly clamped at both extremities. In the experiments the rod was slid over the stainless steel rod that could allow small displacements of the silicone rubber rod which, in turn, could affect the results.
- In the numerical simulations, the stainless steel rods were considered perfectly rigid. Although the metal rods were considerably stiffer than the silicone rubber rod, small vibrations of the stainless steel rods could affect the dynamics of the problem.
- The Poisson's ratio of the silicone rubber used in the experiment was not known to the supplier, hence the simulations made use of a value commonly available in literature. Some sensitivity analysis on this parameter is, thus, encouraged.
- Despite the fact that modelling the filling water was done by following as closely as possible the reality, considerable uncertainties were still present on some parameters such as the pressure in the filling liquid. Therefore, the authors believe that improving the modelling of the inner water may lead to an overall improvement of the results.
- Given the tight coupling of the rods, and the resulting small hydraulic diameter of the bundle, the bulk velocity is very sensitive to the small dimensional tolerances of the components (diameter of silicone and steel rods as well as Perspex wall thickness) which may lead to an estimated increase of 18%. A more thorough discussion of this issue is provided in Dolfen et al. (2019).
- The water filling may lower the natural frequency of the rod. Minor energy content of the flow pulsations in that frequency range may activate a significant structural response. This behaviour is possibly insufficiently accounted for by the models, thereby explaining the large discrepancy.

Nevertheless, the authors believe that the numerical efforts presented here contribute to improving FSI simulations. Moreover, the available experimental data can be used for other numerical validations.

Acknowledgements

The project has received funding from the Euratom research and training programme 2014-2018 under the grant agreement No. 654935.

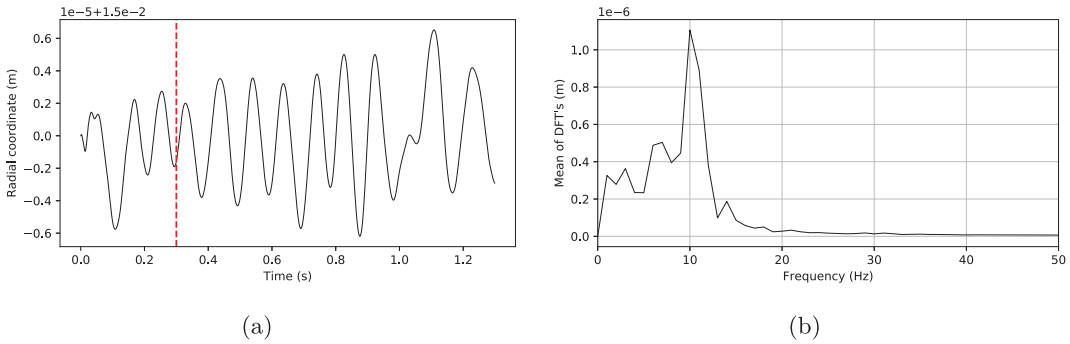

Fig. 16. a) Amplitude of the DFT of the radial velocity component at the 5th point from the central rod. b) Amplitude of the DFT of the axial velocity component at the 8th point from the central rod. Adapted from Dolfen et al. (2019).

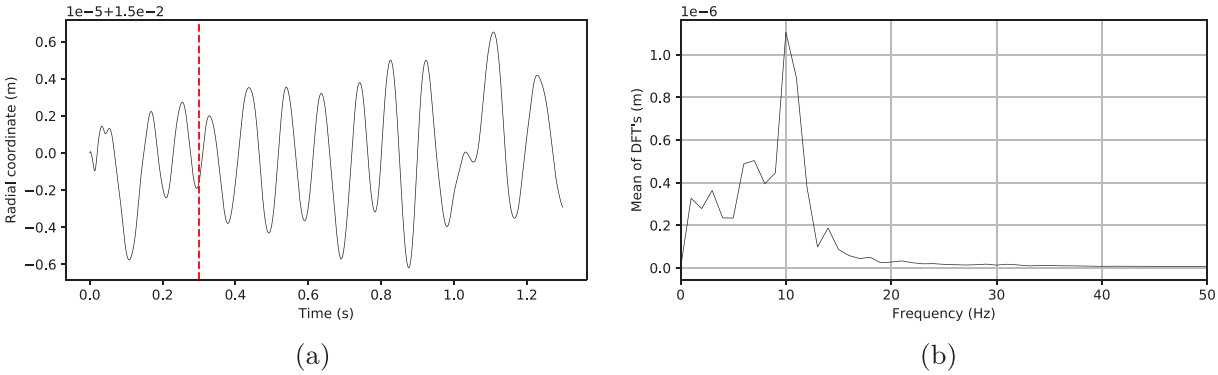

Fig. 17. a) Displacement of a gap-facing point on the surface of the silicone rod versus time. The first 300 time steps (until the red dashed line) are not used for calculating the DFT and root mean square. b) Arithmetic average of the DFTs of the radial deformation of the six gap-facing points on the silicone rod's surface. (For interpretation of the references to colour in this figure legend, the reader is referred to the web version of this article.)

Table 4
Results of the numerical sensitivity study towards the flow rate. Adopted from Dolfen et al. (2019).

Flow rate [ls^{-1}]	Flow pulsation freq. [Hz]	Rod vibration freq. [Hz]	$\bar{\varepsilon}$ [μm]
2.14	10.0	10.0	2.79×10^{-6}
2.53	11.96 − −12.88	12.0	6.49×10^{-6}

Table 5
Summary of the results. Frequencies and mean vibration amplitude $\bar{\varepsilon}$ for both experiment and simulation.

	Flow pulsation freq. [Hz]	Rod vibration freq. [Hz]	$\bar{\varepsilon}$ [μm]
Exp.	7.8	3.8	14.4
NRG	8.6	6.9	5.0
UGhent	10.0	10.0	2.3

The authors wish to express their gratitude to the recently deceased Prof. dr. ir. Jan Vierendeels, for his many contributions to the SESAME project and the field of fluid mechanics.

References

Lexmond, A.S., Mudde, R.F., van der Hagen, T.H.J.J., 2005. Visualisation of the vortex street and characterisation of the cross flow in the gap between two sub-channels. In: Proc. 11th International Topical Meeting on Nuclear Reactor Thermal-Hydraulics Avignon, France.

Mahmood, A., 2011. Single-Phase Crossflow Mixing in a Vertical Tube Bundle Geometry – An Experimental Study. Ph.D. thesis. Delft University of Technology, Delft, The Netherlands.

Tavoularis, S., 2011. Rod bundle vortex networks, gap vortex streets, and gap instability: a nomenclature and some comments on available methodologies. Nucl. Eng. Des. 23, 4612–4614. https://doi.org/10.1016/j.nucengdes.2011.09.043.

Guellouz, M.S., Tavoularis, S., 2000. The structure of turbulent flow in a rectangular channel containing a cylindrical rod – Part 1: Reynolds-averaged measurements. Exp. Thermal Fluid Sci. 23, 59–73. https://doi.org/10.1016/S0894-1777(00)00039-X.

Moradi, H.V., Tavoularis, S., 2019. Flow instability in weakly eccentric annuli. Phys. Fluids 31. https://doi.org/10.1063/1.5093040.

Merzari, E., Ninokata, H., 2011. Proper orthogonal decomposition of the flow in a tight lattice rod-bundle. Nucl. Eng. Des. 241, 4621–4632. https://doi.org/10.1016/j.nucengdes.2010.12.005.

Rayleigh, F.R.S.L., 1879. On the Stability, or Instability, of certain Fluid Motions. In: London Mathematical Society, vol. s1–11. pp. 57–72. https://doi.org/10.1112/plms/s1-11.1.57.

Rowe, D.S., Johnson, B.M., Knudsen, J.G., 1974. Implications concerning rod bundle crossflow mixing based on measurements of turbulent flow structure. Int. J. Heat Mass Transf. 17, 407–419. https://doi.org/10.1016/0017-9310(74)90012-X.

Rehme, K., 1987. The structure of turbulent flow through rod bundles. Nucl. Eng. Des. 99, 141–154. https://doi.org/10.1016/0029-5493(87)90116-6.

Möller, S.V., 1991. On phenomena of turbulent flow through rod bundles. Exp. Thermal Fluid Sci. 4, 25–35. https://doi.org/10.1016/0894-1777(91)90018-M.

Choueiri, G.H., Tavoularis, S., 2014. Experimental investigation of flow development and gap vortex street in an eccentric annular channel. Part 1. Overview of the flow structure. J. Fluid Mech. 725, 521–542. https://doi.org/10.1017/jfm.2014.343.

Choueiri, G.H., Tavoularis, S., 2015. Experimental investigation of flow development and gap vortex street in an eccentric annular channel. Part 2. Effects of inlet conditions, diameter ratio, eccentricity and Reynolds number. J. Fluid Mech. 768, 294–315. https://doi.org/10.1017/jfm.2015.90.

Piot, E., Tavoularis, S., 2011. Gap instability of laminar flows in eccentric annular channels. Nucl. Eng. Des. 241, 4615–4620. https://doi.org/10.1016/j.nucengdes.2010.08.025.

Meyer, L., 2010. From discovery to recognition of periodic large scale vortices in rod bundles as source of natural mixing between subchannels-A review. Nucl. Eng. Des. 240, 1575–1588. https://doi.org/10.1016/j.nucengdes.2010.03.014.

Chang, D., Tavoularis, S., 2005. Unsteady numerical simulations of turbulence and coherent structures in axial flow near a narrow gap. J. Fluids Eng. 127, 458–466. https://doi.org/10.1115/1.1900140.

Chang, D., Tavoularis, S., 2007. Numerical simulation of turbulent flow in a 37-rod bundle. Nucl. Eng. Des. 237, 575–590. https://doi.org/10.1016/j.nucengdes.2006.08.001.

Merzari, E., Ninokata, H., 2009. Anisotropic turbulence and coherent structures in eccentric annular channels. Flow Turbul. Combust. 82, 93–120. https://doi.org/10.1007/s10494-008-9170-2.

Païdoussis, M.P., 2014. Fluid-Structure Interactions – Slender Structures and Axial Flow, vol. 1 Elsevier.

Païdoussis, M.P., 2016. Fluid-Structure Interactions – Slender Structures and Axial Flow, vol. 2 Elsevier.

De Ridder, J., Degroote, J., Van Tichelen, K., Schuurmans, P., Vierendeels, J., 2013. Modal characteristics of a flexible cylinder in turbulent axial flow from numerical simulations. J. Fluid Struct. 43, 110–123. https://doi.org/10.1016/j.jfluidstructs.2013.09.001.

De Ridder, J., Doaré, O., Degroote, J., Van Tichelen, K., Schuurmans, P., Vierendeels, J., 2015. Simulating the fluid forces and fluid-elastic instabilities of a clamped-clamped cylinder in turbulent axial flow. J. Fluid Struct. 55, 139–154. https://doi.org/10.1016/j.jfluidstructs.2015.03.001.

De Santis, D., Shams, A., 2017. Numerical modeling of flow induced vibration of nuclear fuel rods. Nucl. Eng. Des. 320, 44–56. https://doi.org/10.1016/j.nucengdes.2017.05.013.

De Ridder, J., Degroote, J., Vierendeels, J., Van Tichelen, K., 2016. Vortex-induced vibrations by axial flow in a bundle of cylinders. Proc. Int. Conf. on Flow-Induced Vibrations, The Hague, The Netherlands.

Idel'chik, I.E., 1966. Handbook of Hydraulic Resistance. Israel Program for Scientific Translations.

Dominguez-Ontiveros, E.E., Hassan, Y.A., 2009. Non-intrusive experimental investigation of flow behavior inside a 5×5 rod bundle with spacer grids using PIV and MIR. Nucl. Eng. Des. 239, 888–898. https://doi.org/10.1016/j.nucengdes.2009.01.009.

Bertocchi, F., Rohde, M., Kloosterman, J.L., 2018. LDA measurements of coherent flow structures and cross-flow across the gap of a compound channel with two half-rods. Nucl. Eng. Des. 326, 17–30. https://doi.org/10.1016/j.nucengdes.2017.10.023.

Mayo, W.T., 1974. A discussion of limitations and extensions of power spectrum estimation with burst counter LDV systems. In: Proc. 2nd Int. Work. on Laser Velocimetry, pp. 90–101.

Tummers, M.J., Passchier, D.M., 2001. Spectral analysis of biased LDA data. Meas. Sci. Technol. 12, 1641–1650. https://doi.org/10.1088/0957-0233/12/10/304.

Tummers, M.J., Passchier, D.M., 1996. Spectral analysis of Individual Realization LDA data, Rept. LR 808. Delft University of Technology, Faculty of Aerospace Engineering, Delft, NL.

Adrian, R.J., Yao, C.S., 1986. Power spectra of fluid velocities measured by laser Doppler velocimetry. Exp. Fluids 5, 17–28. https://doi.org/10.1007/BF00272419.

Nobach, H., 2002. Local time estimation for the slotted correlation function of randomly sampled LDA data. Exp. Fluids 32, 337–345. https://doi.org/10.1007/s003480100362.

Otsu, N., 1979. A threshold selection method from gray-level histograms. IEEE Trans. Syst. Man Cybern. 62–66.

Monson, H.H., 1996. Statistical Digital Signal Processing and Modeling. John Wiley & Sons.

Bertocchi, F., Rohde, M., Kloosterman, J.L., 2019. Experimental investigation on the influence of gap vortex streets on fluidstructure interactions in hexagonal bundle geometries. Int. J. Heat Fluid Flow 79. https://doi.org/10.1016/j.ijheatfluidflow.2019.108443.

Nieuwstadt, F.T.M., Boersma, B.J., Westerweel, J., 2015. Turbulence – Introduction to Theory and Applications of Turbulent Flows. Springer.

Meyer, L., Rehme, K., 1995. Periodic vortices in flow through channels with longitudinal slots or fins. In: Proc. 10th Symp. on Turbulent shear flows.

STAR CCM+ v, 2016. 11.06 User s Guide.

Merzari, E., Ninokata, H., Baglietto, E., 2008. Numerical simulation of flows in tight-lattice fuel bundles. Nucl. Eng. Des. 238, 1703–1719. https://doi.org/10.1016/j.nucengdes.2008.01.001.

SESAME, 2017. Deliverable D1.10, Tech. rep., EU.

Dolfen, H., Bertocchi, F., Rohde, M., Degroote, J., 2019. Numerical simulations of vortex-induced vibrations in a 7-rod bundle compared to experimental data. Proc. SESAME International Workshop, Petten, The Netherlands.